Large- and Small-Signal Average-Value Modeling of Dual-Active-Bridge DC–DC Converter With Triple-Phase-Shift Control

Peng Wang, Xianzhong Chen, Chaonan Tong, Pengyu Jia, *Member, IEEE*, and Chunxue Wen

***Abstract*—This article presents a novel reduced order average model for dual-active-bridge converter which can be applied to all modulation methods, such as single-phase-shift modulation, dual-phase-shift modulation, extended-phase-shift modulation and triple-phase-shift modulation. This model considers conduction, inductance, and transformer power losses. Furthermore, the input–output filters are suitable for system performance analysis. Based on the large-signal average model, the small-signal model and the output transfer function are derived. The detailed model for predicting the large-signal transient is established and the small signal analysis in frequency domain is carried out. This model can accurately predict the steady-state and transient-state response of the system. The experimental results agreed well with the simulation results which proved the accuracy and correctness of the model.**

***Index Terms*—Dual-active-bridge (DAB) converter, input–output filter, large and small signal, power losses, reduced order average model (RAVM).**

I. Introduction

DC MICROGRID connects the distributed generation and main grid which is convenient for the access of distributed generation. As the indispensable interface circuit in dc microgrid, bidirectional dc–dc converter plays an important role in dc microgrid which can effectively improve the utilization of distributed power and the power quality of dc microgrid. The dual-active-bridge (DAB) [1] converter is suitable for soft switching and module cascade [2], [3] in dc microgrid system application based on the features of higher power density, input and output electrical isolation, two-way power flow. It has great application potential and development prospect [3]–[6].

The common characteristic of the DAB converter modulation methods including single-phase-shift (SPS) modulation [7], dual-phase-shift (DPS) modulation [8], extended-phase-shift (EPS) modulation [9], and triple-phase-shift (TPS) modulation [10] is that the transmission power is controlled by changing the relative phase shift of driving signals between and within the bridge arms of DAB converter. SPS modulation is the simplest since there is only one control variable. Hence, for each determined transmission power, there is only one control variable corresponding to it. Correspondingly, the effective value and peak value of inductance current are also uniquely determined. However, the voltage transmission ratio and transmission power of the converter of this method are limited. When the load is light or the voltage transmission ratio is small, the current stress and current effective value of the converter will increase rapidly, and the soft switching range will be reduced. Therefore, SPS modulation method has great limitations [11]–[13]. In order to overcome the limitations of SPS modulation, many literatures have optimized DPS modulation mode [14] and EPS modulation mode [9], [15] in order to reduce reflux power [14], [15] and current stress [14]. However, since DPS modulation and EPS modulation are special forms of TPS modulation, the optimal strategy applied in the definition domain of DPS modulation and EPS modulation is only a local optimal solution. The result can be further improved while the global optimal solution can be obtained using TPS control mode. Hence, the optimal control effect can be achieved. Therefore, the model of DAB converter in TPS modulation mode has more general practical significance.

Modeling of the converter is the basis for the controller design and optimization of the converter which is helpful for the design of the dc system. The state-space average model [15] is the most widely used dc–dc converter modeling method. However, since the DAB converter utilizes a high-frequency transformer to isolate the input and output ports, there is only ac component in the inductor current which does not meet the small ripple assumption required by the state-space average modeling method [16]. Hence, other modeling methods are required.

In the literatures, there are two methods applied in average modeling for DAB converter. Based on Fourier analysis on the main working waveforms of the converter, the first one keeps the

---

Manuscript received September 21, 2020; revised December 9, 2020; accepted January 12, 2021. Date of publication January 19, 2021; date of current version May 5, 2021. This work was supported in part by the National Natural Science Foundation of China under Grant 51907002, in part by the Research on the Key Control Strategy of Cut-Through In-Phase Power Supply System Based on Cascade Multilevel Converters under Grant 51777002, and in part by the Multimodule Interconnection Operation Control and Fault Self-Contained Technology Research of Power Electronic Equipment, Subproject of National Key Research and Development Plan under Grant 2018YFB1503005.02. Recommended for publication by Associate Editor F. W. Fuchs. *(Corresponding author: Xianzhong Chen.)*

Peng Wang is with the University of Science and Technology Beijing, Beijing 100083, China, and also with the North China University of Technology, Beijing 100144, China (e-mail: catdapeng2008@163.com).

Xianzhong Chen and Chaonan Tong are with the University of Science and Technology Beijing, Beijing 100083, China (e-mail: cxz@ustb.edu.cn; tcn@ies.ustb.edu.cn).

Pengyu Jia and Chunxue Wen are with the North China University of Technology, Beijing 100144, China (e-mail: jpynba@hotmail.com; wcx@ncut.edu.cn).

Color versions of one or more figures in this article are available at https://doi.org/10.1109/TPEL.2021.3052459.

Digital Object Identifier 10.1109/TPEL.2021.3052459

fundamental wave and the specific harmonic term and eliminates the switching frequency ac component of the transformer current, and then reduces the order of the state variables [17]–[21]. However, power losses are not considered in this process. The second method increases the order of the state variable and extracts the transient component of the transformer current to form full-order model which including discrete time [22] or continuous time [23]. Specifically, for continuous full-order model, the real part and imaginary part of the transformer current are utilized as state variables to increase the equation order [23]. Generally speaking, the accuracy of full-order model is higher than the reduced-order model [22]. However, the full-order model which is derived from the generalized average model is based on the first-order harmonic. This means that if there is a large harmonic distortion, the accuracy will be impaired [24]. Therefore, in order to accurately reflect the characteristics of the system, it is necessary to retain the higher order harmonic components. However, this will increase the model order and complicate the form, so that the difficulty in practical application is increased.

The main objective of this article is to present and develop a simple, effective, and accurate DAB converter model which can be applied in the full load operating range utilizing different modulation strategies and operating modes. TPS modulation has three degrees of freedom which is the most basic form of phase-shifting control. By adjusting the mathematical relationship of the three degrees of freedom, SPS modulation, DPS modulation, and EPS modulation can all be normalized to TPS modulation control mode and regarded as a special form of TPS modulation.

The above statement is mathematically proven in this article, and a large-signal average model and small-signal model is derived from this concept. The modeling in [25] is based on the TPS modulation method, if the input–output filter circuit is considered, it will benefit the practical engineering application. Zhang *et al.* [26] consider the input–output filter circuits, but the modeling is based on SPS modulation modeling. The average model proposed in this article considers the power losses of conduction, inductance, transformer, and input–output filter which is very useful for system-level research. Based on the large-signal average model, the small-signal model and the output transfer function are derived. The detailed model for predicting the large-signal transient is established and the small-signal analysis in frequency domain is carried out. The model can accurately predict the steady-state and transient response of the DAB converter. Simulation and experimental results show that the model has high accuracy and verifies the correctness of the analysis conclusion.

II. Detailed Switching Modeling of DAB Converter

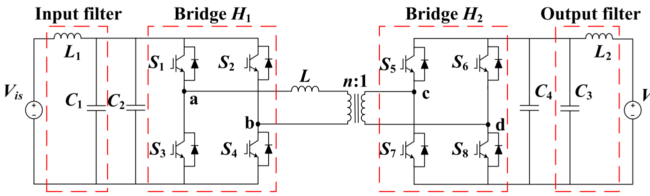

Fig. 1. DAB converter topology.

The main circuit of DAB converter topology is shown in Fig. 1, taking power transmitting from bridge H_1 to bridge H_2 as an example, switching device S_1–S_4 forms the full bridge H_1 of primary side inverter, switching device S_5–S_8 forms the full bridge H_2 of secondary side rectifier, H_1 and H_2 are connected by a magnetic network composed of inductance L and transformer, wherein the electric inductance L can be connected with the auxiliary inductance and the transformer leakage inductance. The high-frequency transformer ratio is n:1, the ac side voltage of bridge H_1 is u_{ab}, the ac side voltage of bridge H_2 is u_{cd}, and the dc voltage of input port and output port are $V_{\rm is}$ and $V_{\rm os}$, respectively, $d_1 \cdot T_{hs}$ is the phase shift between switching device S_1 and S_4, $d_2 \cdot T_{hs}$ is the phase shift between switching device S_1 and S_5, $d_3 \cdot T_{hs}$ is the phase shift between switching device S_1 and S_8, where $T_{\rm hs}$ is the half switch cycle which satisfies the requirements $T_{\rm hs} = T_s/2 = 1/2f_s$, and f_s is the switch frequency.

In the TPS control, there are three independent phase-shift variables d_1, d_2, and d_3, so there are six kinds of phase-shift relations in total. However, it can be analyzed that whether the phase-shift variable d_2 is greater or less than d_3, the same ac output voltage and inductance current waveform can be obtained, and the same transmission power expression can be derived from it. Therefore, the phase-shift d_2 and d_3 are equivalent. Furthermore, the phase-shift relationship of DAB converter can be simplified into three types: $0 \leq d_1 \leq d_2 \leq d_3 \leq 1$, $0 \leq d_2 \leq d_1 \leq d_3 \leq 1$, and $0 \leq d_2 \leq d_3 \leq d_1 \leq 1$, the main working waveforms of DAB converter are shown in Fig. 2. The system loss is ignored in the steady state of the system, and the output power P can be expressed as shown in (1), in this article, the case of $0 \leq d_1 \leq d_2 \leq d_3 \leq 1$ is taken as an example for modeling, and the other cases will not be given further elaboration since they are similar to each other

$$p = \frac{P}{P_N} = \begin{cases} 2\left(-d_1 + d_2 + d_3 - d_1^2 - d_2^2 - d_3^2 + d_1 d_2 + d_2 d_3\right) \\ \qquad (0 \leq d_1 \leq d_2 \leq d_3 \leq 1) \\ 2\left(-d_1 + d_2 + d_3 - d_3^2 + d_1 d_3 - d_1 d_2\right) \\ \qquad (0 \leq d_2 \leq d_1 \leq d_3 \leq 1) \\ 2\left(-d_1 + d_2 + d_3 + d_1^2 - d_1 d_2 - d_1 d_3\right) \\ \qquad (0 \leq d_2 \leq d_3 \leq d_1 \leq 1) \end{cases} \tag{1}$$

where $P = \frac{1}{T_s}\int_0^{T_s} U_{ab}(t) i_l(t) dt$ and $P_N = \frac{nT_s V_{\rm in} V_{\rm os}}{8L_{\rm eq}}$.

This article considers that the input–output filter is a typical LC filter and RC damping circuit is used to suppress voltage and current ripple. At the same time, the excitation inductance L_M, equivalent resistance R_M, leakage inductance L_{l1} and L_{l2}, equivalent resistance R_{l1} and R_{l2} of the core, equivalent resistance R_{cu} of auxiliary inductance L_k, and MOSFET resistance R_s are considered. The equivalent resistance and inductance of the primary side can be expressed as

$$R_{\rm eq} = R_{l1} + 2R_{s1} + n^2 \left(R_{l1} + 2R_{s2}\right) + R_{\rm cu} \tag{2}$$

$$L_{\rm eq} = L_{l1} + n^2 \cdot L_{l2} + L_k. \tag{3}$$

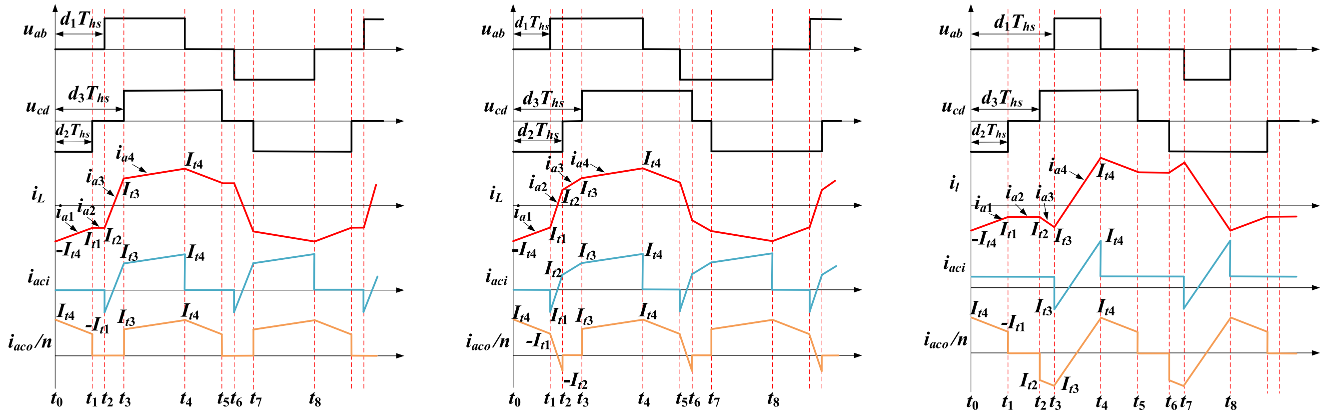

(a) (b) (c)

Fig. 2. Main operating waveforms of DAB converter. (a) $0 \le d_1 \le d_2 \le d_3 \le 1$. (b) $0 \le d_2 \le d_1 \le d_3 \le 1$. (c) $0 \le d_2 \le d_3 \le d_1 \le 1$.

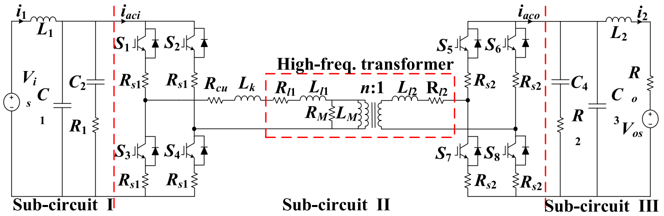

Fig. 3. Detailed switching model of DAB converter.

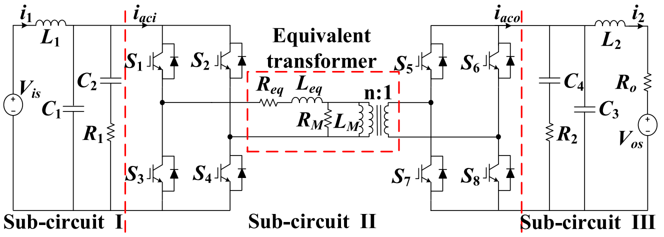

Fig. 4. Equivalent detailed switching model of DAB converter.

Combining R_{eq} and L_{eq}, a detailed switching modeling is obtained, as shown in Fig. 3.

III. AVM OF DAB CONVERTER

A. Steady-State Equation of DAB Converter

As shown in Fig. 4, the converter circuit can be divided into three parts, and the formula is as follows:

$$\begin{cases} L_1\frac{di_1}{d\tau} = v_{\mathrm{is}} - v_{\mathrm{c}1} \\ L_2\frac{di_2}{d\tau} = v_{\mathrm{c}3} - v_{\mathrm{os}} - i_2R_o \\ C_2\frac{dv_{c2}}{d\tau} = \frac{v_{c1}-v_{c2}}{R_1} \\ C_4\frac{dv_{c4}}{d\tau} = \frac{v_{c3}-v_{c4}}{R_2} \\ C_1\frac{dv_{c1}}{d\tau} = i_1 - i_{\mathrm{aci}} - \frac{v_{c1}-v_{c2}}{R_1} \\ C_3\frac{dv_{c3}}{d\tau} = i_{\mathrm{aco}} - i_2 - \frac{v_{c3}-v_{c4}}{R_1} \end{cases} \tag{4}$$

where $v_{\mathrm{c}1}$, $v_{\mathrm{c}2}$, $v_{\mathrm{c}3}$, and $v_{\mathrm{c}4}$ are the voltages of capacitor C_1, C_2, C_3, and C_4, respectively; i_{aci} and i_{aco} are the average values of input and output current corresponding to subcircuit II, respectively; τ is used to denote the time within a half of switching period. As shown in Fig. 2(a), input and output current contain a large number of periodic variables instead of transient variables, and reduced order average model (RAVM) uses the average value. Assuming the excitation inductance and resistance (L_M and R_M) currents are ignored, the i_{aci} equation is expressed as

$$i_{\mathrm{aci}} = \begin{cases} i_{a1} = \frac{V'_{\mathrm{c}3}}{R_{\mathrm{eq}}} + \left(-I_{t4} - \frac{V'_{\mathrm{c}3}}{R_{\mathrm{eq}}}\right) e^{-\frac{Req}{Leq}\tau} \; (0 \le \tau < d_1T_{\mathrm{hs}}) \\ i_{a2} = \frac{V_{c1}+V'_{\mathrm{c}3}}{R_{\mathrm{eq}}} + \left(I_{t1} - \frac{V_{c1}+V'_{\mathrm{c}3}}{R_{\mathrm{eq}}}\right) e^{-\frac{R_{\mathrm{eq}}}{L_{\mathrm{eq}}}(\tau-d_1T_{\mathrm{hs}})} \\ \qquad (d_1T_{\mathrm{hs}} \le \tau < d_2T_{\mathrm{hs}}) \\ i_{a3} = \frac{V_{c1}}{R_{\mathrm{eq}}} + \left(I_{t2} - \frac{V_{c1}}{R_{\mathrm{eq}}}\right) e^{-\frac{R_{\mathrm{eq}}}{L_{\mathrm{eq}}}(\tau-d_2T_{hs})} \\ \qquad (d_2T_{\mathrm{hs}} \le \tau < d_3T_{\mathrm{hs}}) \\ i_{a4} = \frac{V_{c1}-V'_{c3}}{R_{\mathrm{eq}}} + \left(I_{t3} - \frac{V_{c1}-V'_{\mathrm{c}3}}{R_{\mathrm{eq}}}\right) e^{-\frac{R_{\mathrm{eq}}}{L_{\mathrm{eq}}}(\tau-d_3T_{\mathrm{hs}})} \\ \qquad (d_3T_{\mathrm{hs}} \le \tau < T_{\mathrm{hs}}) \end{cases} \tag{5}$$

where $V'_{\mathrm{c}3} = nV_{c3}$; and I_{t1}, I_{t2}, I_{t3}, and I_{t4} are the auxiliary inductance current at t_1, t_2, t_3, and t_4, respectively, as shown in Fig. 2(a). Assuming the voltage ripple of V_{c1} and V_{c3} are very small and the voltage is constant in the whole cycle T_{s}, further analysis shows that

$$\begin{cases} i_{a1}\left(d_1T_{hs}\right) = I_{t1} \\ i_{a2}\left(d_2T_{hs}\right) = I_{t2} \\ i_{a3}\left(d_3T_{hs}\right) = I_{t3} \\ i_{a1}\left(T_{hs}\right) = I_{t4} \\ i_{a1}\left(0\right) = -I_{t4}. \end{cases} \tag{6}$$

Above all, I_{t1}, I_{t2}, I_{t3}, and I_{t4} can be derived as

$$I_{t1} = \frac{\frac{nV_{c3}}{R_{\mathrm{eq}}} - \frac{V_{c1}}{R_{\mathrm{eq}}}e^{-\frac{R_{\mathrm{eq}}}{L_{\mathrm{eq}}}d_1T_{\mathrm{hs}}} - \frac{nV_{c3}}{R_{\mathrm{eq}}}e^{-\frac{R_{\mathrm{eq}}}{L_{\mathrm{eq}}}(1+d_1-d_2)T_{\mathrm{hs}}}}{1+e^{-\frac{Req}{Leq}T_{hs}}} + \frac{-\frac{nV_{c3}}{R_{\mathrm{eq}}}e^{-\frac{R_{\mathrm{eq}}}{L_{\mathrm{eq}}}(1+d_1-d_3)T_{\mathrm{hs}}} + \frac{V_{c1}+nV_{c3}}{R_{\mathrm{eq}}}e^{-\frac{R_{\mathrm{eq}}}{L_{\mathrm{eq}}}T_{\mathrm{hs}}}}{1+e^{-\frac{R_{\mathrm{eq}}}{L_{\mathrm{eq}}}T_{\mathrm{hs}}}} \tag{7}$$

$$I_{t2} = \frac{\frac{V_{c1}+nV_{c3}}{R_{eq}} - \frac{V_{c1}}{R_{eq}}e^{-\frac{Req}{Leq}d_2T_{hs}} - \frac{V_{c1}}{R_{eq}}e^{-\frac{Req}{Leq}(d_2-d_1)T_{hs}}}{1+e^{-\frac{Req}{Leq}T_{hs}}}$$

$$+\frac{-\frac{nV_{c3}}{R_{eq}}e^{-\frac{R_{eq}}{L_{eq}}(1+d_2-d_3)T_{hs}}+\frac{V_{c1}}{R_{eq}}e^{-\frac{R_{eq}}{L_{eq}}T_{hs}}}{1+e^{-\frac{R_{eq}}{L_{eq}}T_{hs}}} \tag{8}$$

$$I_{t3}=\frac{\frac{V_{c1}}{R_{eq}}-\frac{V_{c1}}{R_{eq}}e^{-\frac{R_{eq}}{L_{eq}}d_3T_{hs}}-\frac{V_{c1}}{R_{eq}}e^{-\frac{R_{eq}}{L_{eq}}(d_3-d_1)T_{hs}}}{1+e^{-\frac{R_{eq}}{L_{eq}}T_{hs}}}$$
$$+\frac{\frac{nV_{c3}}{R_{eq}}e^{-\frac{R_{eq}}{L_{eq}}(d_3-d_2)T_{hs}}+\frac{V_{c1}-nV_{c3}}{R_{eq}}e^{-\frac{R_{eq}}{L_{eq}}T_{hs}}}{1+e^{-\frac{R_{eq}}{L_{eq}}T_{hs}}} \tag{9}$$

$$I_{t4}=\frac{\frac{V_{c1}-nV_{c3}}{R_{eq}}-\frac{V_{c1}}{R_{eq}}e^{-\frac{R_{eq}}{L_{eq}}(1-d_1)T_{hs}}+\frac{nV_{c3}}{R_{eq}}e^{-\frac{R_{eq}}{L_{eq}}(1-d_2)T_{hs}}}{1+e^{-\frac{R_{eq}}{L_{eq}}T_{hs}}}$$
$$+\frac{\frac{nV_{c3}}{R_{eq}}e^{-\frac{R_{eq}}{L_{eq}}(1-d_3)T_{hs}}-\frac{nV_{c3}}{R_{eq}}e^{-\frac{R_{eq}}{L_{eq}}T_{hs}}}{1+e^{-\frac{R_{eq}}{L_{eq}}T_{hs}}}. \tag{10}$$

As shown in Fig. 2(a), the average values of i_{aci} and i_{aco}/n in the whole cycle T_{s} can be, respectively, expressed as

$$i_{aci}=\frac{1}{T_{hs}}\left(\int_0^{d_1T_{hs}}0d\tau+\int_{d_1T_{hs}}^{d_2T_{hs}}i_{a2}d\tau\right.$$
$$\left.+\int_{d_2T_{hs}}^{d_3T_{hs}}i_{a3}d\tau+\int_{d_3T_{hs}}^{T_{hs}}i_{a4}d\tau\right) \tag{11}$$

$$\frac{1}{n}\cdot i_{aco}=\frac{1}{T_{hs}}\left(\int_0^{d_1T_{hs}}(-i_{a1})\,d\tau+\int_{d_1T_{hs}}^{d_2T_{hs}}(-i_{a2})\,d\tau\right.$$
$$\left.+\int_{d_2T_{hs}}^{d_3T_{hs}}0d\tau+\int_{d_3T_{hs}}^{T_{hs}}i_{a4}d\tau\right) \tag{12}$$

Substitutions of (5) into (11) and (12) yield

$$T_{hs}\cdot i_{aci}=\frac{V_{c1}+nV_{c3}}{R_{eq}}(d_2-d_1)\,T_{hs}-\frac{L_{eq}}{R_{eq}}$$
$$\times\left(I_{t1}-\frac{V_{c1}+nV_{c3}}{R_{eq}}\right)\left[e^{-\frac{R_{eq}}{L_{eq}}(d_2-d_1)T_{hs}}-1\right]$$
$$+\frac{V_{c1}}{R_{eq}}(d_3-d_2)\,T_{hs}-\frac{L_{eq}}{R_{eq}}\left(I_{t2}-\frac{V_{c1}}{R_{eq}}\right)$$
$$\times\left[e^{-\frac{R_{eq}}{L_{eq}}(d_3-d_2)T_{hs}}-1\right]$$
$$+\frac{V_{c1}-nV_{c3}}{R_{eq}}(1-d_3)\,T_{hs}-\frac{L_{eq}}{R_{eq}}\left(I_{t3}-\frac{V_{c1}-nV_{c3}}{R_{eq}}\right)$$
$$\times\left[e^{-\frac{R_{eq}}{L_{eq}}(1-d_3)T_{hs}}-1\right] \tag{13}$$

$$T_{hs}\cdot\frac{1}{n}\cdot i_{aco}=-\frac{nV_{c3}}{R_{eq}}d_1T_{hs}-\frac{L_{eq}}{R_{eq}}\left(I_{t4}+\frac{nV_{c3}}{R_{eq}}\right)$$
$$\left(e^{-\frac{R_{eq}}{L_{eq}}d_1T_{hs}}-1\right)$$
$$-\frac{V_{c1}+nV_{c3}}{R_{eq}}(d_2-d_1)\,T_{hs}+\frac{L_{eq}}{R_{eq}}\left(I_{t1}-\frac{V_{c1}+nV_{c3}}{R_{eq}}\right)$$
$$\left[e^{-\frac{R_{eq}}{L_{eq}}(d_2-d_1)T_{hs}}-1\right]$$
$$+\frac{V_{c1}-nV_{c3}}{R_{eq}}(1-d_3)\,T_{hs}-\frac{L_{eq}}{R_{eq}}\left(I_{t3}-\frac{V_{c1}-nV_{c3}}{R_{eq}}\right)$$
$$\left[e^{-\frac{R_{eq}}{L_{eq}}(1-d_3)T_{hs}}-1\right]. \tag{14}$$

Regardless of transformer core losses and excitation inductance losses, (4), (7)–(10), (11), and (12) constitute RAVM.

B. Effect of Magnetizing Inductance and Core losses

In the model defined in (4), (7)–(10), (11), and (12), the magnetizing current through L_M and R_M is not considered, actually, L_M and R_M will draw a low current from the power source to generate loss. In addition, the magnetization and demagnetization of the inductance L_M are synchronous with the commutation of the bridge with a period of $2T_{\text{hs}}$. Therefore, the averaging value of i_{aco} should be taken in $2T_{\text{hs}}$, and (12) is modified as

$$\frac{1}{n}\cdot i_{aco}=\frac{1}{2T_{hs}}\left[2\int_0^{d_1T_{hs}}(-i_{a1})\,d\tau+2\int_{d_1T_{hs}}^{d_2T_{hs}}(-i_{a2})\,d\tau\right.$$
$$\left.+2\int_{d_2T_{hs}}^{d_3T_{hs}}0d\tau+2\int_{d_3T_{hs}}^{T_{hs}}i_{a4}d\tau\right]$$
$$-\frac{1}{2T_{hs}}\int_0^{2T_{hs}}i_Md\tau-\frac{n\cdot V_{c3}}{R_M} \tag{15}$$

where i_M is the current in auxiliary inductance L_M; moreover, the average value of i_M should be zero in one cycle of steady state, i.e.,

$$\int_0^{2T_{hs}}i_Md\tau=0. \tag{16}$$

Therefore, L_M does not affect the modeling of DAB converter, and (24) can be further simplified as follows:

$$\frac{1}{n}\cdot i_{aco}=\frac{1}{2T_{hs}}\left[2\int_0^{d_1T_{hs}}(-i_{a1})\,d\tau+2\int_{d_1T_{hs}}^{d_2T_{hs}}(-i_{a2})\,d\tau\right.$$
$$\left.+2\int_{d_3T_{hs}}^{T_{hs}}i_{a4}d\tau\right]-\frac{n\cdot V_{c3}}{R_M}. \tag{17}$$

Considering the losses of core and magnetizing inductance, the RAVM is defined as (4), (7)–(10), (11), and (17). Note that the RAVM of DAB converter proposed in this article is suitable for PSM. However, in many applications, the combination of PSM and PWM is used [8], [28]. In this case, the expression of i_{aci} which is different from (11) should be derived again. Nevertheless, the analysis method adopted in this article is still applicable to the RAVM derivation when different modulation schemes are used.

C. RAVM Circuit of DAB Converter

The proposed RAVM circuit is shown in Fig. 5, where the variable values are defined as (4), (7)–(10), (11), and (17). Here, the current i_{aci} and i_{aco}/n are represented as independent current sources, and the transformer is considered as an ideal dc transformer (proportional variable). Since there are no switching

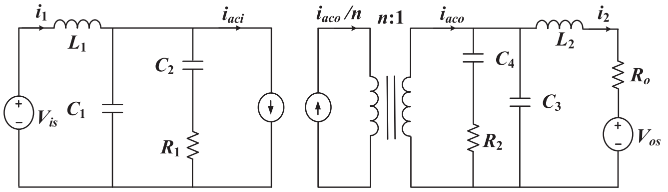

Fig. 5. Proposed reduced-order average circuit model of DAB converter.

devices in the proposed RAVM, the implementation, and simulation will be much faster than the detailed model. Small-signal model and frequency-domain analysis can also be obtained by linearization.

IV. SMALL-SIGNAL MODEL OF DAB

In order to construct a small-signal ac model at a dc operating point, it is assumed that the variables v_{is}, v_{os} and d_1, d_2, d_3 are equal to their quiescent values plus their respective superimposed small ac perturbations, i.e.,

$$\begin{cases} v_{is} = V_{is} + \hat{v}_{is} \\ v_{os} = V_{os} + \hat{v}_{os} \\ d_1 = D_1 + \hat{d}_1 \\ d_2 = D_2 + \hat{d}_2 \\ d_3 = D_3 + \hat{d}_3. \end{cases} \tag{18}$$

The output average variables $i_1, i_2, v_{c1}, v_{c2}, v_{c3}$, and v_{c4} will also be equal to their corresponding quiescent values plus their respective superimposed small ac variables, i.e.,

$$\begin{cases} i_1 = I_1 + \hat{i}_1 \\ i_2 = I_2 + \hat{i}_2 \\ v_{c1} = V_{c1} + \hat{v}_{c1} \\ v_{c2} = V_{c2} + \hat{v}_{c2} \\ v_{c3} = V_{c3} + \hat{v}_{c3} \\ v_{c4} = V_{c4} + \hat{v}_{c4}. \end{cases} \tag{19}$$

The small-signal model can be obtained by substituting (19) into the previous large-signal average model. In this process, the dc term will be eliminated, and the second and higher order ac terms will be neglected.

Noting that during whole derivation process, there will be equations with $e^{a\hat{d}}$ term, where a is a constant coefficient. According to Taylor series, when $\hat{d}$ is close enough to zero, $e^{a\hat{d}}$ can be expressed as infinite convergence series

$$e^{a\hat{d}} = \sum_{n=0}^{\infty} \frac{\left(a\hat{d}\right)^n}{n!} = 1 + \frac{a}{1!}\hat{d} + \frac{a^2}{2!}\hat{d}^2 + \cdots + \frac{a^n}{n!}\hat{d}^n + \cdots . \tag{20}$$

If the second and higher order terms are ignored, $e^{a\hat{d}}$ approximated as

$$\begin{cases} e^{a\hat{d}_1} = 1 + a\hat{d}_1 \\ e^{a\hat{d}_2} = 1 + a\hat{d}_2 \\ e^{a\hat{d}_3} = 1 + a\hat{d}_3. \end{cases} \tag{21}$$

Using (21) to linearize the average model at a certain operating point, the small-signal model is obtained as

$$\begin{cases} L_1 \frac{d\hat{i}_1}{d\tau} = \hat{v}_{is} - \hat{v}_{c1} \\ L_2 \frac{d\hat{i}_2}{d\tau} = \hat{v}_{c3} - \hat{v}_{os} - \hat{i}_2 R_o \\ C_2 \frac{d\hat{v}_{c2}}{d\tau} = \frac{\hat{v}_{c1} - \hat{v}_{c2}}{R_1} \\ C_4 \frac{d\hat{v}_{c4}}{d\tau} = \frac{\hat{v}_{c3} - \hat{v}_{c4}}{R_2} \\ C_1 \frac{d\hat{v}_{c1}}{d\tau} = \hat{i}_1 - \hat{i}_{aci} - \frac{\hat{v}_{c1} - \hat{v}_{c2}}{R_1} \\ C_3 \frac{d\hat{v}_{c3}}{d\tau} = \hat{i}_{aco} - \hat{i}_2 - \frac{\hat{v}_{c3} - \hat{v}_{c4}}{R_1} \end{cases} \tag{22}$$

$$\underset{aci}{\hat{i}} = p\,\hat{d}_1 + q\,\hat{d}_2 + \gamma\,\hat{d}_3 + \alpha\,\hat{v}_{c1} + \beta\,\hat{v}_{c3} \tag{23}$$

$$\frac{1}{n} \cdot \underset{aco}{\hat{i}} = x\,\hat{d}_1 + y\,\hat{d}_2 + z\,\hat{d}_3 + \eta\,\hat{v}_{c1} + \theta\,\hat{v}_{c3} \tag{24}$$

where

$$p = -\frac{V_{c1} + nV_{c3}}{R_{eq}} + \frac{V_{c1}e^{-\frac{R_{eq}}{L_{eq}}D_1 T_{hs}} + V_{c1}e^{-\frac{R_{eq}}{L_{eq}}(1-D_1)T_{hs}}}{R_{eq}\left(1 + e^{-\frac{R_{eq}}{L_{eq}}T_{hs}}\right)} + \frac{nV_{c3}e^{-\frac{R_{eq}}{L_{eq}}(1+D_1-D_2)T_{hs}} + nV_{c3}e^{-\frac{R_{eq}}{L_{eq}}(1+D_1-D_3)T_{hs}}}{R_{eq}\left(1 + e^{-\frac{R_{eq}}{L_{eq}}T_{hs}}\right)} \tag{25}$$

$$q = \frac{nV_{c3}}{R_{eq}} - \frac{nV_{c3}e^{-\frac{R_{eq}}{L_{eq}}(1-D_2)T_{hs}} + nV_{c3}e^{-\frac{R_{eq}}{L_{eq}}(1+D_1-D_2)T_{hs}}}{R_{eq}\left(1 + e^{-\frac{R_{eq}}{L_{eq}}T_{hs}}\right)} \tag{26}$$

$$\gamma = \frac{nV_{c3}}{R_{eq}} - \frac{nV_{c3}e^{-\frac{R_{eq}}{L_{eq}}(1-D_3)T_{hs}} + nV_{c3}e^{-\frac{R_{eq}}{L_{eq}}(1+D_1-D_3)T_{hs}}}{R_{eq}\left(1 + e^{-\frac{R_{eq}}{L_{eq}}T_{hs}}\right)} \tag{27}$$

$$\alpha = \frac{1 - D_1}{R_{eq}} - \frac{1}{T_{hs}} \cdot \frac{L_{eq}}{R_{eq}} \times \frac{1 + e^{-\frac{R_{eq}}{L_{eq}}D_1 T_{hs}} - e^{-\frac{R_{eq}}{L_{eq}}(1-D_1)T_{hs}} - e^{-\frac{R_{eq}}{L_{eq}}T_{hs}}}{R_{eq}\left(1 + e^{-\frac{R_{eq}}{L_{eq}}T_{hs}}\right)} \tag{28}$$

$$\beta = n \cdot \frac{-1 - D_1 + D_2 + D_3}{R_{eq}} - \frac{n}{T_{hs}} \cdot \frac{L_{eq}}{R_{eq}}$$

$$\cdot \frac{-2+e^{-\frac{R_{eq}}{L_{eq}}(1-D_2)T_{hs}}+e^{-\frac{R_{eq}}{L_{eq}}(1-D_3)T_{hs}}}{R_{eq}\cdot\left(1+e^{-\frac{R_{eq}}{L_{eq}}T_{hs}}\right)}+\frac{n}{T_{hs}}\cdot\frac{L_{eq}}{R_{eq}}$$

$$\cdot \frac{e^{-\frac{R_{eq}}{L_{eq}}(1+D_1-D_2)T_{hs}}+e^{-\frac{R_{eq}}{L_{eq}}(1+D_1-D_3)T_{hs}}-2e^{-\frac{R_{eq}}{L_{eq}}T_{hs}}}{R_{eq}\cdot\left(1+e^{-\frac{R_{eq}}{L_{eq}}T_{hs}}\right)} \tag{29}$$

$$x=\frac{nV_{c3}}{R_{eq}}-\frac{V_{c1}e^{-\frac{R_{eq}}{L_{eq}}(D_2-D_1)T_{hs}}+V_{c1}e^{-\frac{R_{eq}}{L_{eq}}(D_3-D_1)T_{hs}}}{R_{eq}\left(1+e^{-\frac{R_{eq}}{L_{eq}}T_{hs}}\right)} \tag{30}$$

$$y=-\frac{V_{c1}+nV_{c3}}{R_{eq}}+\frac{V_{c1}e^{-\frac{R_{eq}}{L_{eq}}D_2T_{hs}}+V_{c1}e^{-\frac{R_{eq}}{L_{eq}}(D_2-D_1)T_{hs}}}{R_{eq}\left(1+e^{-\frac{R_{eq}}{L_{eq}}T_{hs}}\right)}$$

$$+\frac{nV_{c3}e^{-\frac{R_{eq}}{L_{eq}}(D_3-D_2)T_{hs}}+nV_{c3}e^{-\frac{R_{eq}}{L_{eq}}(1+D_2-D_3)T_{hs}}}{R_{eq}\left(1+e^{-\frac{R_{eq}}{L_{eq}}T_{hs}}\right)} \tag{31}$$

$$z=-\frac{V_{c1}-nV_{c3}}{R_{eq}}+\frac{V_{c1}e^{-\frac{R_{eq}}{L_{eq}}D_3T_{hs}}+V_{c1}e^{-\frac{R_{eq}}{L_{eq}}(D_3-D_1)T_{hs}}}{R_{eq}\left(1+e^{-\frac{R_{eq}}{L_{eq}}T_{hs}}\right)}$$

$$-\frac{nV_{c3}e^{-\frac{R_{eq}}{L_{eq}}(D_3-D_2)T_{hs}}+nV_{c3}e^{-\frac{R_{eq}}{L_{eq}}(1+D_2-D_3)T_{hs}}}{R_{eq}\left(1+e^{-\frac{R_{eq}}{L_{eq}}T_{hs}}\right)} \tag{32}$$

$$\eta=\frac{1+D_1-D_2-D_3}{R_{eq}}+\frac{1}{T_{hs}}\cdot\frac{L_{eq}}{R_{eq}}$$

$$\cdot\frac{2-e^{-\frac{R_{eq}}{L_{eq}}D_2T_{hs}}-e^{-\frac{R_{eq}}{L_{eq}}D_3T_{hs}}}{R_{eq}\left(1+e^{-\frac{R_{eq}}{L_{eq}}T_{hs}}\right)}-\frac{1}{T_{hs}}\cdot\frac{L_{eq}}{R_{eq}}$$

$$\cdot\frac{e^{-\frac{R_{eq}}{L_{eq}}(D_2-D_1)T_{hs}}+e^{-\frac{R_{eq}}{L_{eq}}(D_3-D_1)T_{hs}}-2e^{-\frac{R_{eq}}{L_{eq}}T_{hs}}}{R_{eq}\left(1+e^{-\frac{R_{eq}}{L_{eq}}T_{hs}}\right)} \tag{33}$$

$$\theta=n\cdot\frac{-1-D_2+D_3}{R_{eq}}+\frac{n}{T_{hs}}\cdot\frac{L_{eq}}{R_{eq}}$$

$$\cdot\frac{1-e^{-\frac{R_{eq}}{L_{eq}}(1+D_2-D_3)T_{hs}}+e^{-\frac{R_{eq}}{L_{eq}}(D_3-D_2)T_{hs}}-e^{-\frac{R_{eq}}{L_{eq}}T_{hs}}}{R_{eq}\cdot\left(1+e^{-\frac{R_{eq}}{L_{eq}}T_{hs}}\right)}$$

$$-\frac{1}{R_M}. \tag{34}$$

Based on the derivation in (18)–(34), the small-signal ac circuit model of DAB converter is constructed as the large-signal model shown in Fig. 5.

Frequency domain analysis can also be performed using linearization and subsequent calculations of various transfer functions. If the Laplace transform is applied to (22)–(24), the control-to-output transfer function can be derived as

$$G_{od_1}(s)=\left.\frac{\hat{i}_2(s)}{\hat{d}_1(s)}\right|_{\hat{d}_2(s)=0,\hat{d}_3(s)=0,\hat{v}_{is}(s)=0,\hat{v}_{os}(s)=0}$$

$$=\frac{1}{R_0+L_2s}\cdot\frac{x-\eta p/G_{A1}(s)}{G_{A2}(s)/n+\eta\beta/G_{A1}(s)} \tag{35}$$

$$G_{od_2}(s)=\left.\frac{\hat{i}_2(s)}{\hat{d}_2(s)}\right|_{\hat{d}_1(s)=0,\hat{d}_3(s)=0,\hat{v}_{is}(s)=0,\hat{v}_{os}(s)=0}$$

$$=\frac{1}{R_0+L_2s}\cdot\frac{y-\eta q/G_{A1}(s)}{G_{A2}(s)/n+\eta\beta/G_{A1}(s)} \tag{36}$$

$$G_{od_3}(s)=\left.\frac{\hat{i}_2(s)}{\hat{d}_3(s)}\right|_{\hat{d}_1(s)=0,\hat{d}_2(s)=0,\hat{v}_{is}(s)=0,\hat{v}_{os}(s)=0}$$

$$=\frac{1}{R_0+L_2s}\cdot\frac{z-\eta\gamma/G_{A1}(s)}{G_{A2}(s)/n+\eta\beta/G_{A1}(s)} \tag{37}$$

$$G_{A1}(s)=(1/R_1+C_1s)+\frac{1}{L_1s}+\alpha-\frac{1/R_2}{1+R_1C_2s} \tag{38}$$

$$G_{A2}(s)=(1/R_2+C_3s)+\frac{1}{R_0+L_2s}-n\theta-\frac{1/R_2}{1+R_2C_4s}. \tag{39}$$

Similarly, the control-to-input transfer function can be derived as

$$G_{id_1}(s)=\left.\frac{\hat{i}_1(s)}{\hat{d}_1(s)}\right|_{\hat{d}_2(s)=0,\hat{d}_3(s)=0,\hat{v}_{is}(s)=0,\hat{v}_{os}(s)=0}$$

$$=\frac{1}{L_1s}\cdot\frac{\beta x/G_{A2}(s)+p/n}{G_{A1}(s)/n+\eta\beta/G_{A2}(s)} \tag{40}$$

$$G_{id_2}(s)=\left.\frac{\hat{i}_1(s)}{\hat{d}_2(s)}\right|_{\hat{d}_1(s)=0,\hat{d}_3(s)=0,\hat{v}_{is}(s)=0,\hat{v}_{os}(s)=0}$$

$$=\frac{1}{L_1s}\cdot\frac{\beta y/G_{A2}(s)+q/n}{G_{A1}(s)/n+\eta\beta/G_{A2}(s)} \tag{41}$$

$$G_{id_3}(s)=\left.\frac{\hat{i}_1(s)}{\hat{d}_2(s)}\right|_{\hat{d}_1(s)=0,\hat{d}_2(s)=0,\hat{v}_{is}(s)=0,\hat{v}_{os}(s)=0}$$

$$=\frac{1}{L_1s}\cdot\frac{\beta z/G_{A2}(s)+\gamma/n}{G_{A1}(s)/n+\eta\beta/G_{A2}(s)}. \tag{42}$$

V. MODEL VALIDATION

The table of electrical parameters of DAB converter is listed in Table I, and the experimental prototype is shown in Fig. 6. The detailed model of DAB converter is implemented in PLECS, and

TABLE I
SIMULATION PARAMETERS OF DAB CONVERTER

Parameter	Value	Parameter	Value
v_{is}	400VDC	C_3	150μF
v_{os}	110VDC	C_4	680μF
n	3	R_1	0.157Ω
f_s	25kHz	R_2	0.057Ω
L_k	520μH	R_o	0.1Ω
L_1	110μH	R_{l1}	0.05Ω
L_2	450μH	R_{l2}	0.009Ω
L_{l1}	2.94μH	R_{cu}	0.035Ω
L_{l2}	0.395μH	R_M	3kΩ
L_M	20.77mH	R_{s1}	0.075Ω
C_1	150μF	R_{s2}	0.047Ω
C_2	560μF		

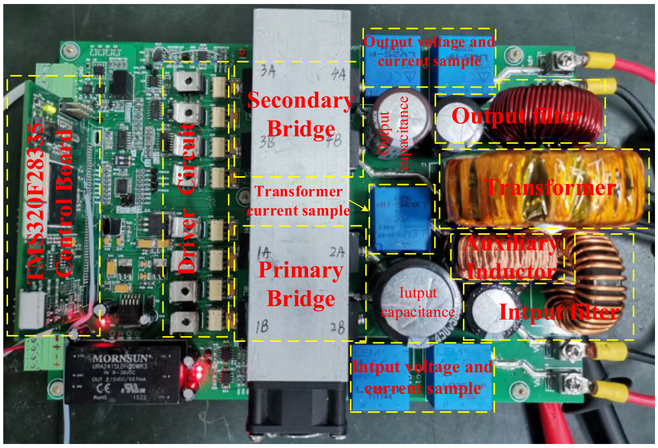

Fig. 6. Photograph of the experimental DAB converter.

the proposed RAVM model is implemented in MATLAB. A prototype is established to verify the RAVM proposed in this article. The experimental DAB converter is designed for dc microgrid power electronic transformer. Each working state contains 107 operating points which are used to verify the average model. These operating points contain all modulation strategies and operation modes. In the small-signal model, the Bode diagram of the control-to-output transfer function is compared with the detailed model simulation and experimental results of each model, and the multifrequency analysis is carried out after the perturbance source and response observer are properly placed in the circuit. In the experimental device, the primary side of the converter is connected to 400 V dc bus (V_{is}), the secondary side is connected to 110 V dc bus (V_{os}) by cable, and the peak current of the secondary side dc bus is 11 A. In the experiment, the primary side dc bus is simulated by programmable dc power supply to provide stable dc voltage. The secondary side dc bus is simulated by power electronic load with power level (as shown in Fig. 6), which is composed of MOSFET, nanocrystalline core high-frequency transformer, and input–output filter. In order to simulate the dynamic response of the cable resistance, the average model and the prototype added a resistor $R_o = 0.1\ \Omega$ to simulate the cable resistance. When the model is applied to the actual system, the actual R_o value cannot be ignored (usually far less than 0.1 Ω). The ratio of the primary core to the secondary core of the experimental DAB converter is 3:1, the rated power

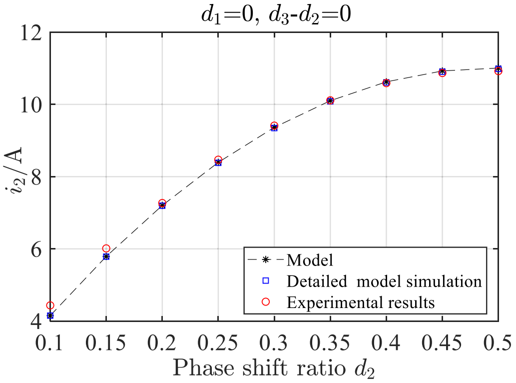

Fig. 7. Comparison of detailed switching model simulation and experimental results with the model for case 1: $d_1 = 0$, d_3–$d_2 = 0$, d_2 is varying.

is 1.21 kW, and the auxiliary inductance $L_{\mathrm{eq}} = 523\ \mu$H. Since the leakage inductor of transformer is very small (2.94 μh), a 520 μH inductor is needed to connect in series to the primary core in order to increase the L_{eq} value. As shown in Table I, the inductance values $L_{l1} = 2.94\ \mu$H and $L_{l2} = 0.395\ \mu$H are used in the model. In the experiment, the 32-bit floating-point microprocessor TMS320F28335 is used, and the clock is 150 MHz to realize the control of DAB converter.

In order to validate the correctness of the average model proposed in this article, different parameters are selected with three freedom degrees to verify that the proposed model is suitable for the average model of SPS modulation, DPS modulation, EPS modulation, and TPS modulation by the following four cases:

A. Case1: Phase-Shift Modulation ($d_1 = 0,0 < d_2 < 1$, d_3–$d_2 = 0$)

1) *RAVM Validation:* The average model is validated and the results from the following subcase are presented: $d_1 = 0$, d_3–$d_2 = 0$, and d_2 is varying. The results from the detailed switching model and experiments are compared with those from the RAVM, as shown in Fig. 7.

2) *Small-Signal-Model Validation:* The small-signal model is validated at the following steady-state operating point: $d_1 = 0$, $d_2 = 0.3$, and $d_3 = 0.3$. The output dc current predicted by the RAVM and the detailed switching model is 9.35 A and the experiment result is 9.41 A. The results from the detailed switching model and experiments are compared with those from the RAVM, as shown in Fig. 8.

B. Case2: Duty-Ratio Modulation for Primary Side ($0 < d_1 < d_2 < 1$, d_3–$d_2 = 0$)

1) *RAVM Validation:* The average model is validated and the results from the following subcase are presented.

a) $d_2 = 0.5$, d_3–$d_2 = 0$, d_1 is varying.
b) $d_1 = 0.1$, d_3–$d_2 = 0$, d_2 is varying.

The results from the detailed switching model and experiments are compared with those from the RAVM, as shown in Fig. 9.

2) *Small-Signal*-Model *Validation:* The small-signal model is validated at the following steady-state operating point: d_1

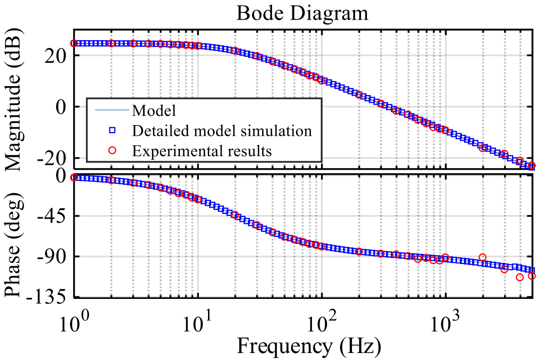

Fig. 8. Comparison of detailed switching model simulation and experimental results with the model for case 1. Control-to-output transfer function with respect to d_2.

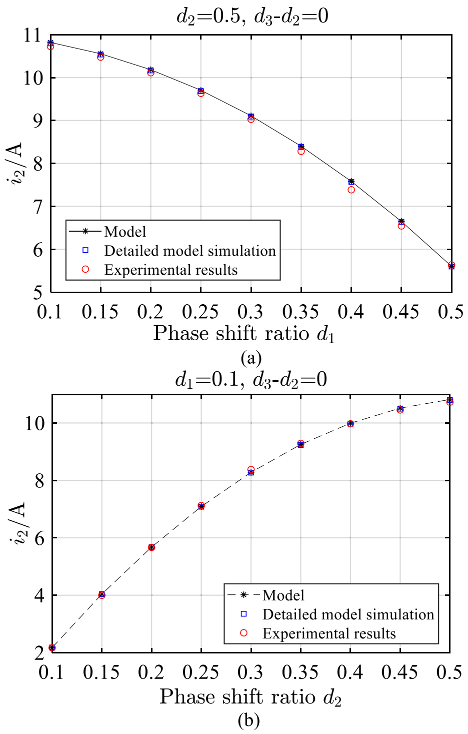

(a)

(b)

Fig. 9. Comparison of detailed switching model simulation and experimental results with the model for case 2. (a) $d_2 = 0.5$, d_3–$d_2 = 0$, d_1 is varying. (b) $d_1 = 0.1$, d_3–$d_2 = 0$, d_2 is varying.

$= 0.1$, $d_2 = 0.3$, and $d_3 = 0.3$. The output current predicted by the RAVM and the detailed switching model is 8.27 A and the experiment result is 8.37 A. The results from the detailed switching model and experiments are compared with those from the RAVM, as shown in Fig. 10.

C. Case3: Duty-Ratio Modulation for Secondary Side ($d_1 = 0$, $0 < d_2 < d_3 < 1$)

1) RAVM Validation: The average model is validated and the results from the following subcase are presented

a) $d_1 = 0$, d_3–$d_2 = 0.2$, d_2 is varying.
b) $d_1 = 0$, $d_2 = 0.5$, d_3 is varying.

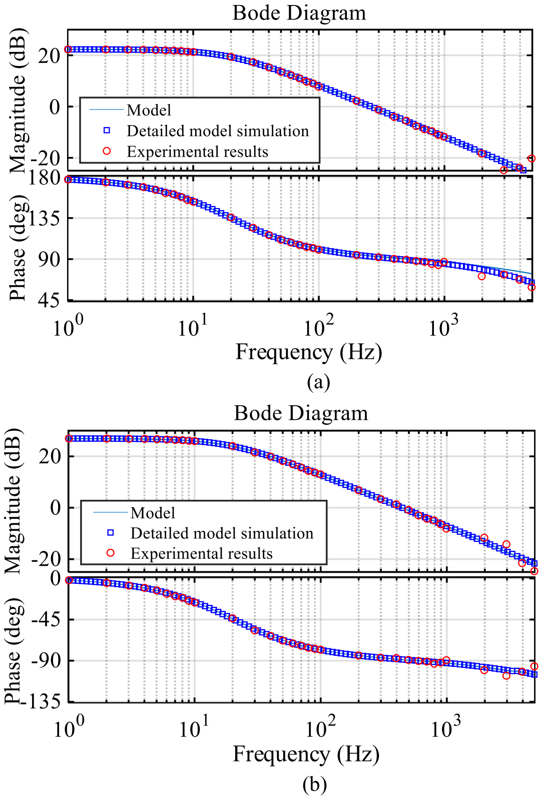

(a)

(b)

Fig. 10. Comparison of detailed switching model simulation and experimental results with the model for case 3. Control-to-output transfer function (a) with respect to d_1 and (b) with respect to d_2.

The results from the detailed switching model and experiments are compared with those from the RAVM, as shown in Fig. 11.

2) Small-Signal-Model Validation: The small-signal model is validated at the following steady-state operating point: $d_1 = 0$, $d_2 = 0.3$, and $d_3 = 0.5$. The output dc current predicted by the RAVM and the detailed switching model is 10.2 A and the experiment result is 10.25 A. The results from the detailed switching model and experiments are compared with those from the RAVM, as shown in Fig. 12.

D. Case4: Duty-Ratio Modulation for Both Sides ($0 < d_1 < d_2 < d_3 < 1$)

1) RAVM Validation: The average model is validated and the results from the following subcase are presented

a) $d_2 = 0.5$, $d_3 = 0.7$, d_1 is varying.
b) $d_1 = 0.1$, d_3–$d_2 = 0.2$, d_2 is varying.
c) $d_1 = 0.1$, $d_2 = 0.5$, d_3 is varying.

The results from the detailed switching model and experiments are compared with those from the RAVM, as shown in Fig. 13.

2) Small-Signal-Model Validation: The small-signal model is validated at the following steady-state operating point: $d_1 = 0.2$, $d_2 = 0.5$, $d_3 = 0.7$. The output dc current predicted by the RAVM and the detailed switching model is 10.33 A and in the experiment result is 10.29 A. The results from the detailed

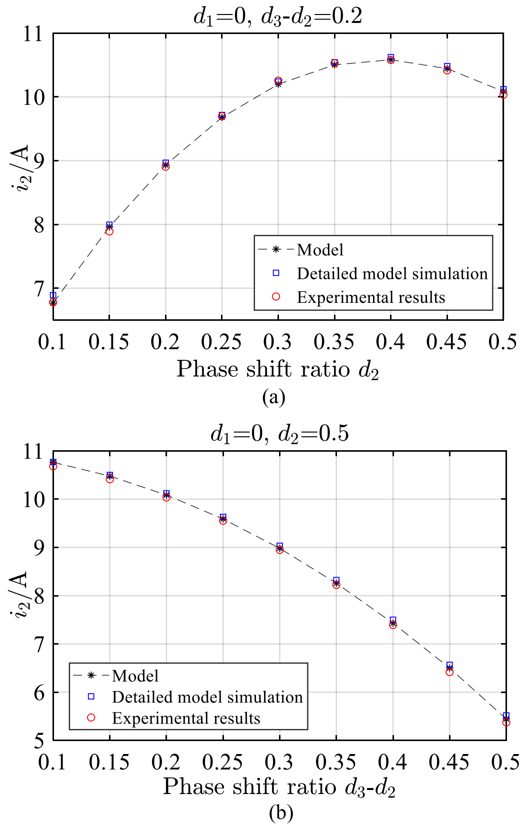

(a)

(b)

Fig. 11. Comparison of detailed switching model simulation and experimental results with the model for case 3. (a) $d_1 = 0$, d_3–$d_2 = 0.2$, d_2 is varying. (b) $d_1 = 0$, $d_2 = 0.5$, d_3 is varying.

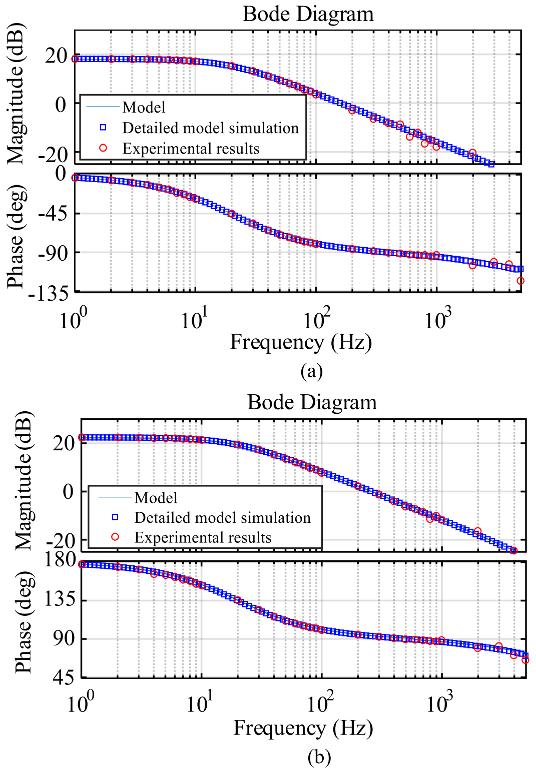

(a)

(b)

Fig. 12. Comparison of detailed switching model simulation and experimental results with the model for case 3. Control-to-output transfer function (a) with respect to d_2 and (b) with respect to d_3.

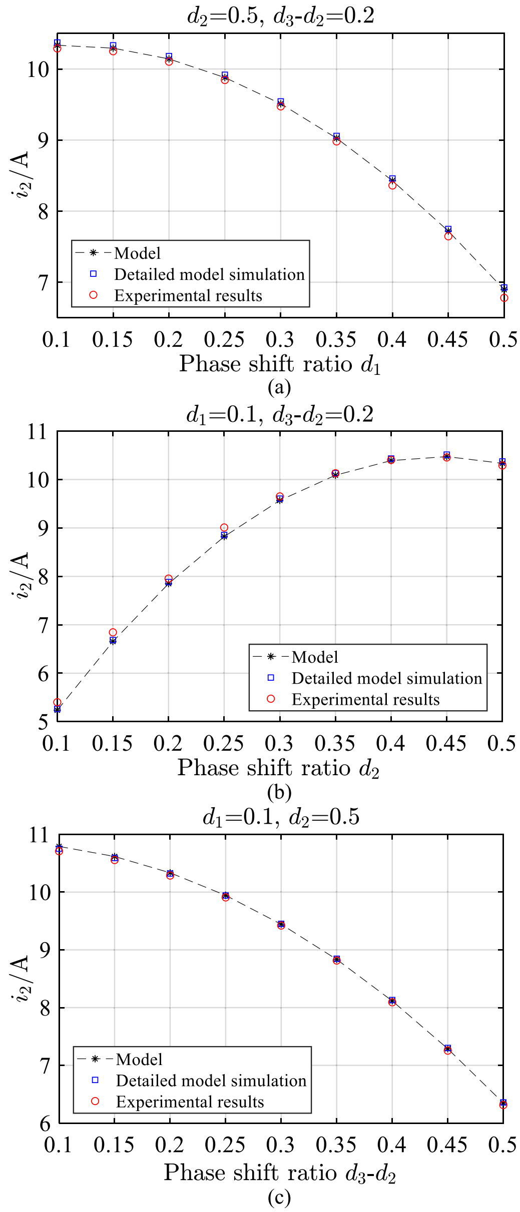

(a)

(b)

(c)

Fig. 13. Comparison of detailed switching model simulation and experimental results with the model for case 4. (a) $d_2 = 0.5$, d_3–$d_2 = 0.2$, d_1 is varying. (b) $d_1 = 0.1$, d_3–$d_2 = 0.2$, d_2 is varying. (c) $d_1 = 0.1$, $d_2 = 0.5$, d_3 is varying.

switching model and experiments are compared with those from the RAVM, as shown in Fig. 14.

VI. OPEN-LOOP EXPERIMENT

A. *Dynamic Response*

In this section, assuming the initial steady-state operating point of the converter is $d_1 = 0.1$, $d_2 = 0.3$, $d_3 = 0.5$, at $t = 0.1$ s, the given values of the control variables are changed, respectively. d_1 increases from 0.1 to 0.3, d_2 and d_3 unchanged, as d_1 increases, the effective duty ratio of u_{ab} voltage decreases. Concurrently, the output current i_2 and transformer current i_{tr} decrease; d_2 increases from 0.3 to 0.5, d_1 and d_3–d_2 remain unchanged. As d_2 increases, the phase-shift ratio between bridge

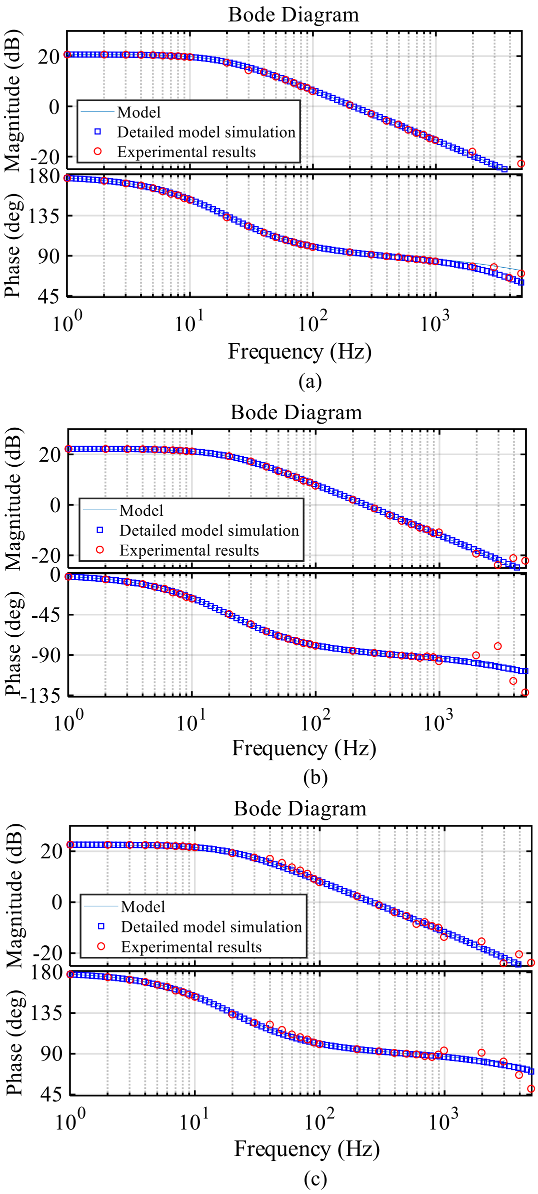

Fig. 14. Comparison of detailed switching model simulation and experimental results with the model for case 4. Control-to-output transfer function (a) with respect to d_1, (b) with respect to d_2, and (c) with respect to d_3.

arms increases. At the same time, the output current i_2 and transformer current i_{tr} increases; d_3 increases from 0.5 to 0.6, d_1 and d_2 remain unchanged. As d_3 increases, the effective duty ratio of u_{cd} voltage decreases, simultaneously, the output current i_2 and transformer current i_{tr} decreases. As shown in Fig. 15, the detailed switching model is in good agreement with the experimental results, so the transformer current of the proposed RAVM and output current i_2 of the detailed model are excluded. The mismatch between the two models and the experimental results is mainly due to the fact that the high-order parasitic parameters (series resistance of skin effect, parasitic capacitance, etc.) in the actual circuit which are not considered in the model.

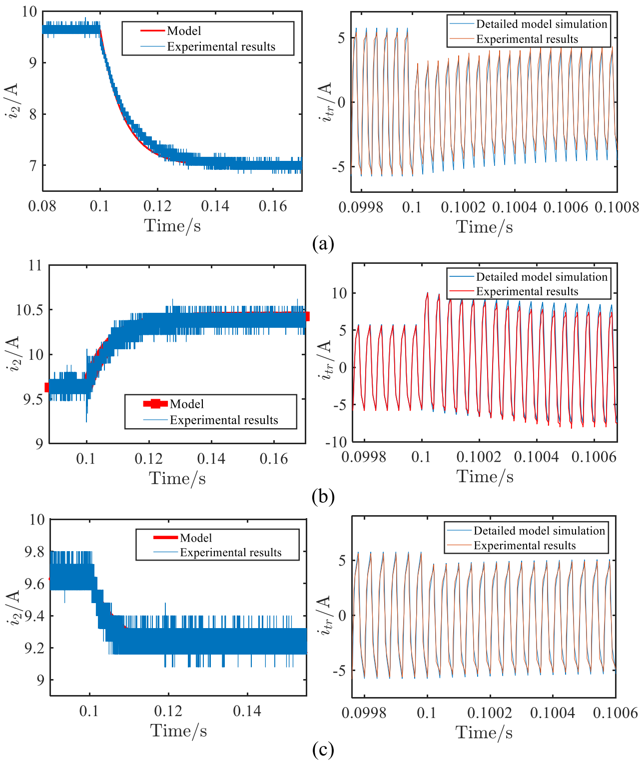

Fig. 15. Output current and transformer current transients with a phase-shift change. (a) $d_2 = 0.5$, d_3–$d_2 = 0.2$, d_1 is varying. (b) $d_1 = 0.1$, d_3–$d_2 = 0.2$, d_2 is varying. (c) $d_1 = 0.1$, $d_2 = 0.5$, d_3 is varying.

B. Frequency Response Analysis

In this section, the frequency domain analysis is carried out at the static operating points with $d_1 = 0.2$, $d_2 = 0.5$, and $d_3 = 0.7$ and the results from the following subcase are presented.

1) The sum of d_1 and small-signal perturbance, $d_2 = 0.5$, $d_3 = 0.7$.
2) The sum of d_2 and small-signal perturbance, $d_1 = 0.2$, $d_3 - d_2 = 0.2$.
3) The sum of d_3 and small-signal perturbance, $d_1 = 0.2$, $d_2 = 0.5$.

In the model, $V_{\text{is}} = 400$ V, $V_{\text{os}} = 110$ V. The experimental results also verify the correctness of the analysis. In the experiment, a small disturbance $d_{1\text{sin}}$, $d_{2\text{sin}}$, and $d_{3\text{sin}}$ are added to the static point of phase-shift ratio separately. At this point, the actual phase-shift ratio becomes a function of time t, i.e.,

$$d_1(t) = D_1 + d_{1\,\sin}(t) \qquad d_{1\,\sin}(t) = A_{m1}\sin 2\pi f_{p1}t \quad (43)$$

$$d_2(t) = D_2 + d_{2\,\sin}(t) \qquad d_{2\,\sin}(t) = A_{m2}\sin 2\pi f_{p2}t \quad (44)$$

$$d_3(t) = D_3 + d_{3\,\sin}(t) \qquad d_{3\,\sin}(t) = A_{m3}\sin 2\pi f_{p3}t \quad (45)$$

where $A_{m1} = A_{m2} = A_{m3} = 0.02$ is the amplitude and f_p ranging from 1 to 5 kHz is the frequency of disturbance $d_{1\text{sin}}$, $d_{2\text{sin}}$, and $d_{3\text{sin}}$. Note that in the experiment, due to the use of digital controller, the time counter of TMS320F28335 controller has a minimum time resolution of 6.67 ns, and the minimum rate of variation of d_1, d_2, and d_3 is $\Delta d_{\min} = 6.67\ \text{ns}/20\ \mu s = 3.33\times 10^4$, so the level of d_1, d_2, and d_3 cannot be changed continuously.

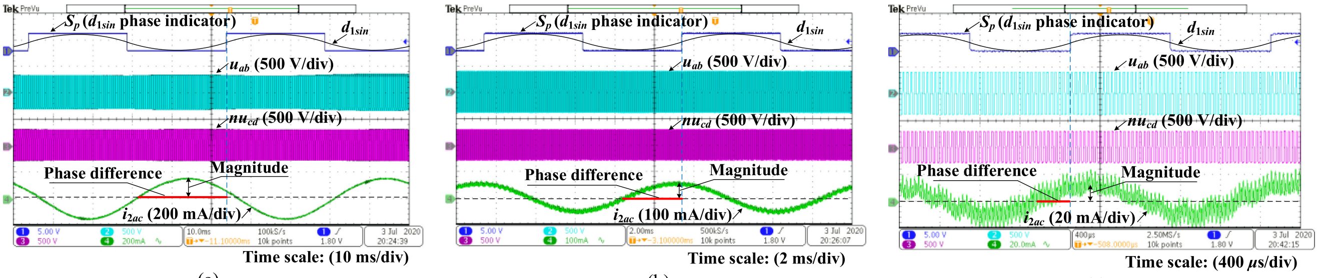

(a) (b) (c)

Fig. 16. Illustration of frequency-response measurements with $D_1 = 0.2$, $D_2 = 0.5$, $D_3 = 0.7$, and various f_{p1} values. (a) $f_{p1} = 20$ Hz. (b) $f_{p1} = 100$ Hz. (c) $f_{p1} = 500$ Hz.

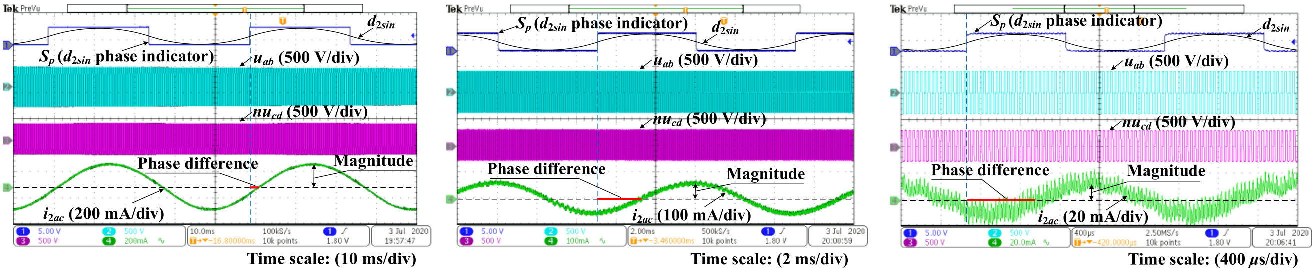

(a) (b) (c)

Fig. 17. Illustration of frequency-response measurements with $D_1 = 0.2$, $D_2 = 0.5$, $D_3 = 0.7$, and various f_{p2} values. (a) $f_{p2} = 20$ Hz. (b) $f_{p2} = 100$ Hz. (c) $f_{p2} = 500$ Hz.

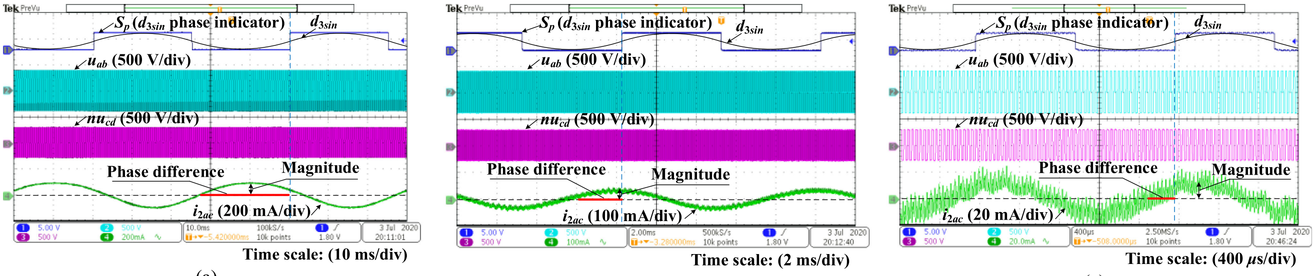

(a) (b) (c)

Fig. 18. Illustration of frequency-response measurements with $D_1 = 0.2$, $D_2 = 0.5$, $D_3 = 0.7$, and various f_{p3} values. (a) $f_{p3} = 20$ Hz. (b) $f_{p3} = 100$ Hz. (c) $f_{p3} = 500$ Hz.

When A_{m1}, A_{m2}, and A_{m3} are set to 0.02, d_1, d_2, and d_3 may have $2A_{m1}/\Delta d_{\min} = 120$ horizontal resolutions which is enough to measure, the measurement of frequency response is shown in Figs. 16–18, and the amplitude frequency response is obtained from the peak value of the measured i_2 waveform; the phase response is obtained by measuring the phase difference between the part of i_2 and the $d_{1\text{sin}}$, $d_{2\text{sin}}$, and $d_{3\text{sin}}$ signals represented by the square wave signal S_p. It should be noted that when the frequency of disturbance $d_{1\text{sin}}$, $d_{2\text{sin}}$, and $d_{3\text{sin}}$ are greater than 700 Hz, the amplitude of A_m should be increased due to the design of output filter parameters, that is, $A_{m1} = A_{m2} = A_{m3} = 0.06$.

C. Power Loss and Efficiency Analysis

In order to analyze the power losses and efficiency of the model, taking cases 1 and 4 in Section V, for example, the model steady-state predictions, the detailed model simulation, and the experimental results are compared in Fig. 19. Specifically, the power losses and the efficiency of the DAB converter with different phase-shift ratios are plotted. Fig. 19(a) corresponding to the case 1, Fig. 19(b)–(d) corresponding to the case 4. Considering the inside impedance of the secondary power source, the efficiency η' is calculated through:

$$\eta' = V_o \cdot i_2 / (V_{in} \cdot i_1) \tag{46}$$

$$V_{in} = V_{is} \tag{47}$$

$$V_o = V_{os} + i_2 \cdot R_o \tag{48}$$

where the variables are defined in Fig. 4. It is noted that DAB converter are commonly operating in zero-voltage-switching (ZVS) mode. Therefore, the switching loss is not considered in this article. For an ideal DAB without parasitic resistances, $V_{\text{is}} : nV_{\text{os}} = 1$ should be ensured in order that ZVS operation can

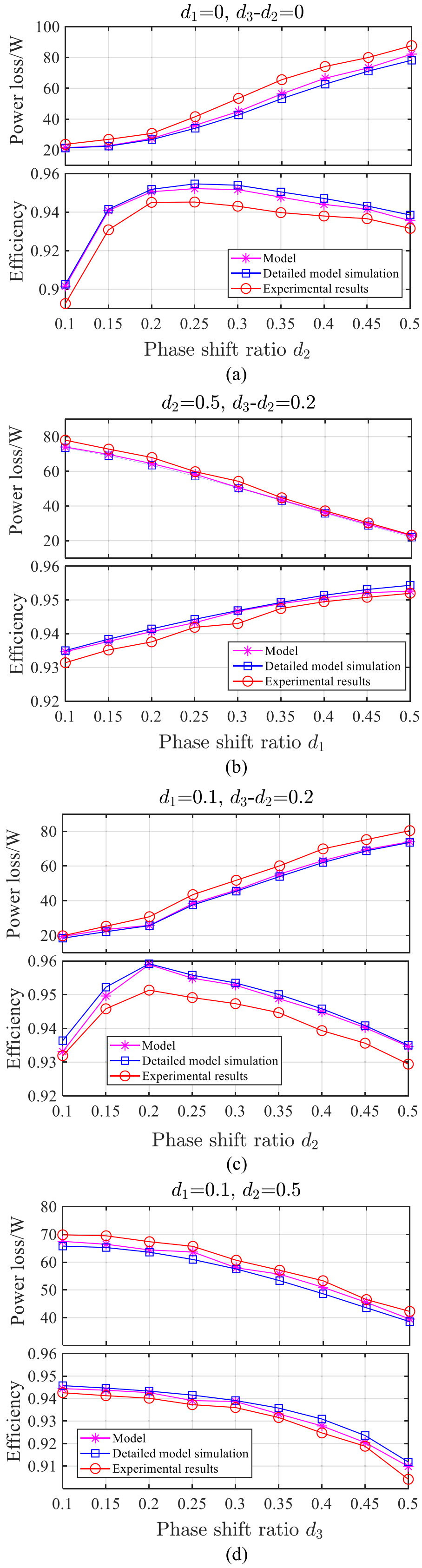

Fig. 19. Power loss and efficiency varied with the steady-state operating points under different working modes. (a) $d_1 = 0$, d_3–$d_2 = 0$, d_2 is varying. (b) $d_2 = 0.5$, $d_3 = 0.7$, d_1 is varying. (c) $d_1 = 0.1$, d_3–$d_2 = 0.2$, d_2 is varying. (d) $d_1 = 0.1$, $d_2 = 0.5$, d_3 is varying.

be achieved. At the same time, the current of the transformer is lowest. In the prototype, due to the existence of R_{eq} and R_o, the actual voltage ratio of the DAB is lower than $V_{\mathrm{is}} : nV_{\mathrm{os}}$. For this reason, ZVS operation is achievable when $V_{\mathrm{is}} : nV_{\mathrm{os}}$ is slightly higher than 1 in the experiment. According to the parameters of the experimental prototype in Table I, $V_{\mathrm{is}} : nV_{\mathrm{os}}$ is 1.21 in this article. For the different phase-shift ratios, namely the different output active power, the efficiency of the RAVM is basically consistent with the detailed switching model since the proposed RAVM includes the majority of power losses in the circuit. Due to the presence of unpredictable circuit and PCB conduction losses, the efficiency of the prototype is slightly lower than that predicted by the RAVM.

VII. DISCUSSION

1) *Average Model*

The simulation results of the detailed switching model are in good agreement with the prediction results of the RAVM for all operating points in four cases and different subcases, and the experimental results match closely to the RAVM. A small mismatch between these two models and the experimental results are mainly due to the high-order parasitic parameters (series resistance of skin effect, parasitic capacitance, etc.) in the actual circuit and the dead time of the complementary power electronic switching devices. According to the direction of the current, when the semiconductor device is turned ON, the dead time may lead to the increase or decrease of the voltage duty ratios of the bridge voltage. Furthermore, the dead time may also increase or decrease the phase shift between the voltage duty ratios of the bridge voltage and their commanded value.

2) *Large-Signal Open-Loop Dynamic Response*

Fig. 16(a)–(c) shows the large-signal transient response to a step change in d_1, d_2, and d_3, and the same controller is used to realize control function. The figures show good agreement between the large-signal responses obtained from experiments and those predicted from the proposed RAVM and detailed switching model. The mismatch between the two models and the experimental results is mainly due to the fact that the high-order parasitic parameters (series resistance of skin effect, parasitic capacitance, etc.) in the actual circuit are not considered in the model. The transformer current of the proposed RAVM and output current i_2 of the detailed model are excluded as the detailed switching model simulation results are difficult to distinguish from the RAVM results.

3) *Small-Signal Model*

The small-signal model predicts a pole at 15 Hz, which is determined by the load resistance and output filter circuit. In all cases, the experimental results are in good agreement with the RAVM results and the detailed switching model, although the experimental results start to deviate from the stage more than 2 kHz. This mismatch may be due to the poles introduced by the output filter. If these poles are known accurately, they can be considered in the model.

4) Potential Applications

There are several possible applications of the proposed model. For instance, in [27], the modeling and control of a DAB converter with input–output filters is presented. The small-signal model derived from the average DAB converter was employed to state the transfer functions. However, the small-signal model does not include the input–output filter circuit. In this case, the proposed model may be used to derive modified closed-loop transfer functions.

Similarly, the proposed model is suitable for systems with no input–output filter circuit or only input or output filter circuit. In [28] and [29], only the input filter circuit is included, for the design of the whole system controller, the filter circuit needs to be considered separately. The model proposed in this article only needs to rewrite formula (4) and (22), and other derivation processes are the same. Thus, the model can simplify the design process of the system controller.

The proposed model may also be applied to assess the performance of control structures, where, typically, the operating regions and modulation strategies are divided into modes and submodes. For instance, in [30], the full model of DAB with TPS control was classified into six operating modes. Afterwards, the concept of global optimal condition equations is proposed to derive the closed form of analytic expressions of an optimal modulation scheme that makes the DAB converter operate with minimized root-mean-square current during whole power range with different operating modes, but the proposed model will eliminate the need to have separate plant models for such analyses.

E. Remarks

The RAVM can accurately predict the steady-state and transient response of the DAB converter with TPS control system. Simulation and experimental results show that the model can accurately predict the output current, transformer current, and large-signal transient behavior of the converter. Modeling and simulations of DAB converters can be extremely useful prior to hardware implementations as they help component selection and preliminary evaluation of the overall dc system.

VIII. CONCLUSION

In this article, a novel RAVM for DAB converter is proposed, the main power losses (including conduction and transformer losses) and input–output filter are considered in this method. Based on the large-signal RAVM, the small-signal model and the control output transfer function are derived. The derivation shows that the Taylor series method is very effective for the linearization analysis of RAVM. Time domain simulation and experimental results of the DAB converter prototype proved the effectiveness of the RAVM and small-signal model. The model calculation results and detailed switching model simulation are in good agreement with the experimental results. Therefore, through the parameter selection of three degrees of freedom, the proposed model is suitable for the average model of SPS modulation, DPS modulation, EPS modulation, and TPS modulation, and this model can be used for DAB converter design and analysis.

REFERENCES

[1] M. N. Kheraluwala, R. W. Gascoigne, D. M. Divan, and E. D. Baumann, “Performance characterization of a high-power dual active bridge DC-to-DC converter,” *IEEE Trans. Ind. Appl.*, vol. 28, no. 6, pp. 1294–1301, Nov./Dec. 1992.

[2] H. Akagi, T. Yamagishi, N. M. L. Tan, S. Kinouchi, Y. Miyazaki, and M. Koyama, “Power-loss breakdown of a 750-V 100-kW 20-kHz bidirectional isolated DC–DC converter using SiC-MOSFET/SBD dual modules,” *IEEE Trans. Ind. Appl.*, vol. 51, no. 1, pp. 420–428, Jan./Feb. 2015.

[3] B. Zhao, Q. Song, W. Liu, and Y. Sun, “Overview of dual-active-bridge isolated bidirectional DC–DC converter for high-frequency-link power-conversion system,” *IEEE Trans. Power Electron.*, vol. 29, no. 8, pp. 4091–4106, Aug. 2014.

[4] F. Krismer and J. W. Kolar, “Accurate small-signal model for the digital control of an automotive bidirectional dual active bridge,” *IEEE Trans. Power Electron.*, vol. 24, no. 12, pp. 2756–2768, Dec. 2009.

[5] S. Inoue and H. Akagi, “A bidirectional isolated DC–DC converter as a core circuit of the next-generation medium-voltage power conversion system,” *IEEE Trans. Power Electron.*, vol. 22, no. 2, pp. 535–542, Mar. 2007.

[6] Y. Shi, R. Li, Y. Xue, and H. Li, “Optimized operation of current-fed dual active bridge DC–DC converter for PV applications,” *IEEE Trans. Ind. Electron.*, vol. 62, no. 11, pp. 6986–6995, Nov. 2015.

[7] B. Zhao, Q. Song, and W. Liu, “Power characterization of isolated bidirectional dual-active-bridge DC–DC converter with dual-phase-shift control,” *IEEE Trans. Power Electron.*, vol. 27, no. 9, pp. 4172–4176, Sep. 2012.

[8] B. Zhao, Q. Yu, and W. Sun, “Extended-phase-shift control of isolated bidirectional DC–DC converter for power distribution in microgrid,” *IEEE Trans. Power Electron.*, vol. 27, no. 11, pp. 4667–4680, Nov. 2012.

[9] F. Krismer and J. W. Kolar, “Closed form solution for minimum conduction loss modulation of DAB converters,” *IEEE Trans. Power Electron.*, vol. 27, no. 1, pp. 174–188, Jan. 2012.

[10] A. K. Jain and R. Ayyanar, “PWM control of dual active bridge: Comprehensive analysis and experimental verification,” *IEEE Trans. Power Electron.*, vol. 26, no. 4, pp. 1215–1227, Apr. 2011.

[11] H. Bai, Z. Nie, and C. C. Mi, “Experimental comparison of traditional phase-shift, dual-phase-shift, and model-based control of isolated bidirectional DC–DC converters,” *IEEE Trans. Power Electron.*, vol. 25, no. 6, pp. 1444–1449, Jun. 2010.

[12] F. Krismer and J. W. Kolar, “Efficiency-optimized high-current dual active bridge converter for automotive applications,” *IEEE Trans. Ind. Electron.*, vol. 59, no. 7, pp. 2745–2760, Jul. 2012.

[13] H. Bai and C. Mi, “Eliminate reactive power and increase system efficiency of isolated bidirectional dual-active-bridge DC–DC converters using novel dual-phase-shift control,” *IEEE Trans. Power Electron.*, vol. 23, no. 6, pp. 2905–2914, Nov. 2008.

[14] B. Zhao, Q. Song, W. Liu, and W. Sun, “Current-stress-optimized switching strategy of isolated bidirectional DC–DC converter with dual-phase-shift control,” *IEEE Trans. Ind. Electron.*, vol. 60, no. 10, pp. 4458–4467, Oct. 2013.

[15] R. D. Middlebrook and S. Cuk, “A general unified approach to modelling switching-converter power stages,” in *Proc. IEEE Power Electron. Specialists Conf.*, 1976, pp. 18–34.

[16] F. Krismer and J. W. Kolar, “Accurate small-signal model for the digital control of an automotive bidirectional dual active bridge,” *IEEE Trans. Power Electron.*, vol. 24, no. 12, pp. 2756–2768, Dec. 2009.

[17] H. K. Krishnamurthy and R. Ayyanar, “Building block converter module for universal (ac–dc, dc–ac, dc–dc) fully modular power conversion architecture,” in *Proc. IEEE Power Electron. Specialists Conf.*, 2007, pp. 483–489.

[18] H. Bai, M. Chunting, W. Chongwu, and S. Gargies, “The dynamic model and hybrid phase-shift control of a dual-active-bridge converter,” in *Proc. IEEE Ind. Electron. Conf.*, 2008, pp. 2840–2845.

[19] H. Bai, Z. Nie, and C. C. Mi, “Experimental comparison of traditional phase-shift, dual-phase-shift, and model-based control of isolated bidirectional dc-dc converters,” *IEEE Trans. Power Electron.*, vol. 25, no. 6, pp. 1444–1449, Jun. 2010.

[20] D. Costinett, “Reduced order discrete time modeling of ZVS transition dynamic in the dual active bridge converter,” in *Proc. IEEE Appl. Power Electron. Conf. Expo.*, 2015, pp. 365–370.

[21] B. Farhangi and H. A. Toliyat, “Piecewise linear model for snubberless dual active bridge commutation,” *IEEE Trans. Ind. Appl.*, vol. 51, no. 5, pp. 4072–4078, Sep./Oct. 2015.

[22] C. Zhao, S. D. Round, and J. W. Kolar, “Full-order averaging modelling of zero-voltage-switching phase-shift bidirectional dc-dc converters,” *IET Power Electron.*, vol. 3, no. 3, pp. 400–410, 2010.

[23] H. Qin and J. W. Kimball, “Generalized average modeling of dual active bridge DC-DC converter,” *IEEE Trans. Power Electron.*, vol. 27, no. 4, pp. 2078–2084, Apr. 2012.

[24] J.-R. Sibue, J.-P. Ferrieux, G. Meunier, R. P´eriot, and E. Clavel, “Generalized average model of series–parallel resonant converter with capacitive output filter for high power application,” 2010. [Online]. Available: https://hal.archives-ouvertes.fr/hal-00521993

[25] A. S. S. Shah and S. Bhattacharya, “A simple unified model for generic operation of dual active bridge converter,” *IEEE Trans. Ind. Electron.*, vol. 66, no. 5, pp. 3486–3495, May 2019.

[26] K. Zhang, Z. Shan, and J. Jatskevich, “Large- and small-signal average-value modeling of dual-active-bridge DC–DC converter considering power losses,” *IEEE Trans. Power Electron.*, vol. 32, no. 3, pp. 1964–1974, Mar. 2017.

[27] F. L. F. Marcelino, H. H. Sathler, T. R. de Oliveira, and P. F. Donoso-Garcia, “Modeling and control of a dual active bridge for energy storage in DC microgrid applications,” in *Proc. IEEE 8th Int. Symp. Power Electron. Distrib. Gener. Syst.*, Apr. 2017, pp. 1–8.

[28] Y. Guan, Y. Xie, Y. Wang, Y. Liang, and X. Wang, “An active damping strategy for input impedance of bidirectional dual active bridge DC–DC converter: Modeling, shaping, design, and experiment,” *IEEE Trans. Ind. Electron.*, vol. 68, no. 2, pp. 1263–1274, Feb. 2021.

[29] L. Chen *et al.*, “Predictive control based DC microgrid stabilization with the dual active bridge converter,” *IEEE Trans. Ind. Electron.*, vol. 67, no. 10, pp. 8944–8956, Oct. 2020.

[30] A. Tong, L. Hang, G. Li, X. Jiang, and S. Gao, “Modeling and analysis of a dual-active-bridge-isolated bidirectional DC/DC converter to minimize RMS current with whole operating range,” *IEEE Trans. Power Electron.*, vol. 33, no. 6, pp. 5302–5316, Jun. 2018.

Peng Wang was born in Shanxi Province, China, in 1982. He received the B.S. degree from Taiyuan University of Technology, Taiyuan, China, in 2008, and the M.S. degree from the North China University of Technology, Beijing, China, in 2011, both in electrical engineering. He is currently working toward the Ph.D. degree in control science and engineering with the University of Science and Technology Beijing, Beijing, China.

He is currently a Lecturer with the Collaborative Innovation Center of Key Power Energy-Saving Technologies in Beijing, North China University of Technology, Beijing, China. His research interests include power electronic converter, dc microgrid, and electric machines drives.

Xianzhong Chen received the B.S. and M.S. degrees from the Department of Mechanical and Electrical Engineering, Huainan Institute of Mining and Technology, Huainan, China, in 1989 and 1992, respectively, and the Ph.D. degree from the College of Mechanical and Electrical Engineering, China University of Mining and Technology, Xuzhou, China, in 1996.

He is a Director and a Professor with the Key Laboratory of Knowledge Automation for Industrial Processes of Ministry of Education, School of Automation and Electrical Engineering, University of Science and Technology Beijing, Beijing, China. His research interests include robotics, industrial radar detection, and power electronic converter.

Chaonan Tong was born in Anhui province, China, in 1954. He received the M.S. degree in control science and engineering from the University of Science and Technology Beijing, Beijing, China, in 1983.

In 1976, he was with the University of Science and Technology Beijing, Beijing, China, where he was promoted to a Professor in 1997. He has participated in many major engineering research projects in his main capacity. His research interests include control theory and application, electrical automation control system, and power electronic converter.

Pengyu Jia (Member, IEEE) was born in Hebei Province, China, in 1985. He received the B.S. and Ph.D. degrees in electrical engineering from Beijing Jiaotong University, Beijing, China, in 2008 and 2014, respectively.

He is currently working with the School of Electrical and Control Engineering, North China University of Technology, Beijing, China. His research interests include modeling of dc–dc converter and the corresponding control methods.

Chunxue Wen received the B.S. degree from Inner Mongolia University of Technology, Hohhot, China, the M.S. degree from Wuhan University, Wuhan, China, and the Ph.D. degree from the Institute of Electrical Engineering, Chinese Academy of Sciences, Beijing, China, in 2009.

He is currently an Associate Professor with the School of Electrical and Control Engineering, North China University of Technology, Beijing, China. His research interests include microgrid operation and interface converter control.